Key Points:

- We investigate the variations of ground motions in the Binchuan basin in Northwest Yunnan with a temporary dense array
- The amplitude observed in the low velocity zone across the Chenghai fault is up to 20 times as large as outside stations
- Analyzing seismic site response based on dense array data could be an effective method to constrain fault zone structure

Author Contributions:
Formal analysis: Junhao Song
Investigation: Junhao Song
Project Administration: Hongfeng Yang
Supervision: Hongfeng Yang
Writing – original draft: Junhao Song
Writing – review & editing: Hongfeng Yang

Seismic Site Response Inferred From Records at a Dense Linear Array Across the Chenghai Fault Zone, Binchuan, Yunnan

Junhao Song[1] and **Hongfeng Yang[1,2]**

[1]Earth System Science Programme, Faculty of Science, The Chinese University of Hong Kong, Hong Kong, China, [2]Shenzhen Research Institute, The Chinese University of Hong Kong, Shenzhen, China

Abstract Low-velocity zones (LVZ) in the shallow crust such as basins infilled with unconsolidated sediments could significantly amplify seismic waves and cause intense ground motions. In this study, we estimate the seismic site response in the Binchuan basin across the active Chenghai fault zone in northwest Yunnan Province, Southwest China using data from a large-aperture (∼8 km) dense linear array of 125 three-component seismometers deployed in 2018 for ∼1 month. We observe that local earthquakes with larger epicentral distances tend to produce stronger spatial variability in peak ground velocity (PGV) across the array. The PGV values are overall larger in the middle of the array than the two sides, especially in the horizontal directions, which is consistent with both tomographic and traveltime results. Using both nearby and distant earthquakes, we find that horizontal ground motions from 0.2 to 2 Hz at stations inside the LVZ are up to 20 times as large as that outside, and a more localized zone (∼500 m wide) enclosing the fault surface trace is characterized by broader frequency bands and larger factors of amplification. As the distance from the fault increases, amplification factors become smaller while the lower limit of the amplification frequency band gradually increases. Variations in predicted ground motion from one-dimensional SH-wave modeling reveal amplification and attenuation effects of the LVZ, suggesting that strong lateral heterogeneity should be considered. Our results demonstrate that based on dense array data, analyzing seismic site response is an alternative method to effectively constrain the shallow subsurface fault structure.

Plain Language Summary Seismic site response refers to the effects of local site conditions on arriving seismic waves and is an important factor for precisely predicting ground motions. It could vary considerably around major crustal faults, where numerous ruptures and many other processes have together generated complex subsurface structures. Here we investigate seismic site response with its spatial variability across the Chenghai fault zone in northwest Yunnan Province, Southwest China using a ∼8-km-long dense array of 125 seismometers. We find clear variations in peak ground velocity (PGV) produced from local earthquakes across the array and higher PGV values around the fault. Moreover, the spatial variability in PGV increases with the epicentral distance. From local, regional, and teleseismic earthquake recordings in horizontal directions, we observe that ground motions within the previously identified low-velocity zone are amplified by factors up to 20 between 0.2 and 2 Hz, and a ∼500-m-wide zone near the fault with the strongest amplification effects is newly identified. Predictions using one-dimensional SH-wave modeling and the shear-wave velocity model indicate complicated effects from near-fault subsurface structures on ground motions. Our results suggest seismic site response analysis based on dense array data can help effectively constrain low-velocity structures around active fault zones.

1. Introduction

Ground shaking during earthquakes is critical for seismic hazard assessment and is subject to a number of factors, such as earthquake rupture speed and directivity (e.g., Dunham & Bhat, 2008; Ni et al., 2005; Somerville et al., 1997; Yang et al., 2019; Yao & Yang, 2022), as well as attenuation along the wave paths (e.g., Sahakian et al., 2019; Singh et al., 2006; Yoshimoto et al., 1993). In addition, local site conditions also play an important role in characterizing various types of shaking. For example, it has long been observed that the soft rock and damp soil sites (e.g., sandstone, marsh, made land) typically experience the ground motion of higher intensity and larger amplitude than the nearby solid rock sites based on recordings of large earthquakes (Reid, 1910), explosions (Milne, 1908), or even microseisms (Gutenberg, 1927). Performing like resonators or waveguides, deep

sedimentary basins, crustal fault damage zones, and other near-surface low-velocity layers could trap and amplify the seismic waves, and result in intense and prolonged ground shaking at the surface (e.g., Beck & Hall, 1986; Ben-Zion & Aki, 1990; Chen & Yang, 2020; Gutenberg, 1957; Kurzon et al., 2014; Murphy et al., 1971; Pratt et al., 2017; Qiu et al., 2020; Qiu et al., 2021; Rovelli et al., 2002). Furthermore, low-velocity fault zones have been suggested to promote rupture propagation on the fault, leading to larger rupture extent and slip than those from ruptures in intact rock (Weng et al., 2016), which will worsen the ground shaking in regions with a low-velocity fault zone or sedimentary basin. Therefore, precise estimations of the local site effects are necessary to better predict the ground motion and assess the seismic hazard, especially in regions of high seismic risk.

Broad classification of sites into different categories based on soil types or surface geology might be the simplest way to characterize the site effects on ground motion, but it lacks accuracy because of the relatively flat frequency characteristics of averaged site amplification factors in each category (Kawase, 2003). More recently, some proxy parameters such as the averaged shear velocity in the upper 30 m (Vs_{30}) below ground surface and the site fundamental frequency (f_{peak}) are widely used in the modern empirical ground-motion prediction equations (Hassani & Atkinson, 2016), but they may still undervalue the complexity near the surface of the Earth. 3D numerical simulations have also been used to predict the ground motion amplification over regions such as Los Angeles and Seattle basins (e.g., Day et al., 2008; Frankel et al., 2009; Olsen, 2000; Wirth et al., 2019) with varying earthquake scenarios. In many other areas where the high-resolution subsurface structures are currently unavailable, however, it is impracticable to apply such a forward modeling method.

Comparing spectra of earthquake records at two adjacent sites, known as the standard spectral ratio method, is another popular empirical method to estimate the local site effects. By choosing the site at the bedrock outcrop as the reference, the spectral ratios between the investigated sites and the reference thus can be regarded as the frequency-dependent amplification factors caused by the local site conditions (Steidl et al., 1996). Ever since this method was first introduced by Borcherdt (1970), it has been successfully applied to numerous seismic linear or nonlinear site response studies worldwide. For instance, Pratt et al. (2003) showed that, relative to bedrocks west of the Seattle basin, the thick deposits within the basin amplified 0.2–0.8 Hz weak ground motions from the 1999 Mw 7.6 Chi-Chi earthquake by factors of 8–16. By taking the ratio of horizontal spectra for strong ground motions recorded at one station in the North Anatolian fault zone and another station several hundred meters away from the fault, Wu et al. (2009) observed about the one-fold increase of peak spectral ratio and 20–40% reduction of peak frequency at the moment of the mainshock as well as the postseismic logarithmic recovery lasting for around one day, which is closely related to the temporal variation of shear wave velocity in the shallow part of fault zone (FZ). However, this method requires a reference site to have a flat and time-invariant response spectrum, which limits its applications in some experiments. Then, a non-reference site method using the single-station horizontal-to-vertical spectral ratio (HVSR) was developed to study the local site effects (Nakamura, 1989, 2019). Although by far there is no unifying theory explaining HVSR measurements, it is well acknowledged that its peak frequency is closely related to the resonant frequency (Cox et al., 2020).

For sites less than 1–2 km apart, the ground shaking during earthquakes could have appreciable differences in terms of both amplitude and phase as observed in previous studies (e.g., Borcherdt, 1970; Gutenberg, 1957; Hough et al., 1990; Steidl, 1993), which implies the necessity of site effects analysis with higher spatial resolution. Fortunately, with the increasing installation of dense arrays in recent decades (e.g., Ben-Zion et al., 2015; Huang et al., 2020; Lin et al., 2013; Yang et al., 2020), the ground motion characteristics as well as its spatial variability caused by small basin, narrow fault damage zone and other small-scale structures are investigated (Johnson et al., 2020). Based on data from dense arrays, the fault zone spatial extents and seismic properties such as along the San Jacinto fault zone have been better resolved through the systematic analyses of body wave travel times, fault zone trapped waves and resonance waves, as well as the passive and active tomography (e.g., Lewis et al., 2005; Li & Vernon, 2001; Qiu et al., 2020; Roux et al., 2016; Share et al., 2020; Y. Wang et al., 2019; Yang et al., 2014; Yang & Zhu, 2010). The fault damage zones imaged from these studies are less than 1 km wide. Whereas using an ∼8-km-long dense linear array across the Chenghai fault zone, Yang et al. (2020) found a low-velocity-zone (LVZ) of 3.4 km in width and ∼1.5 km in-depth, which was then interpreted to be the sediments controlled by the Chenghai fault. Although the LVZ along the Chenghai fault may not be the fault damage zone, probably due to lack of recent ruptures, strong lateral variations of geometric structures and elastic properties revealed by the dense array pose great challenges to the seismic hazard assessment in this region.
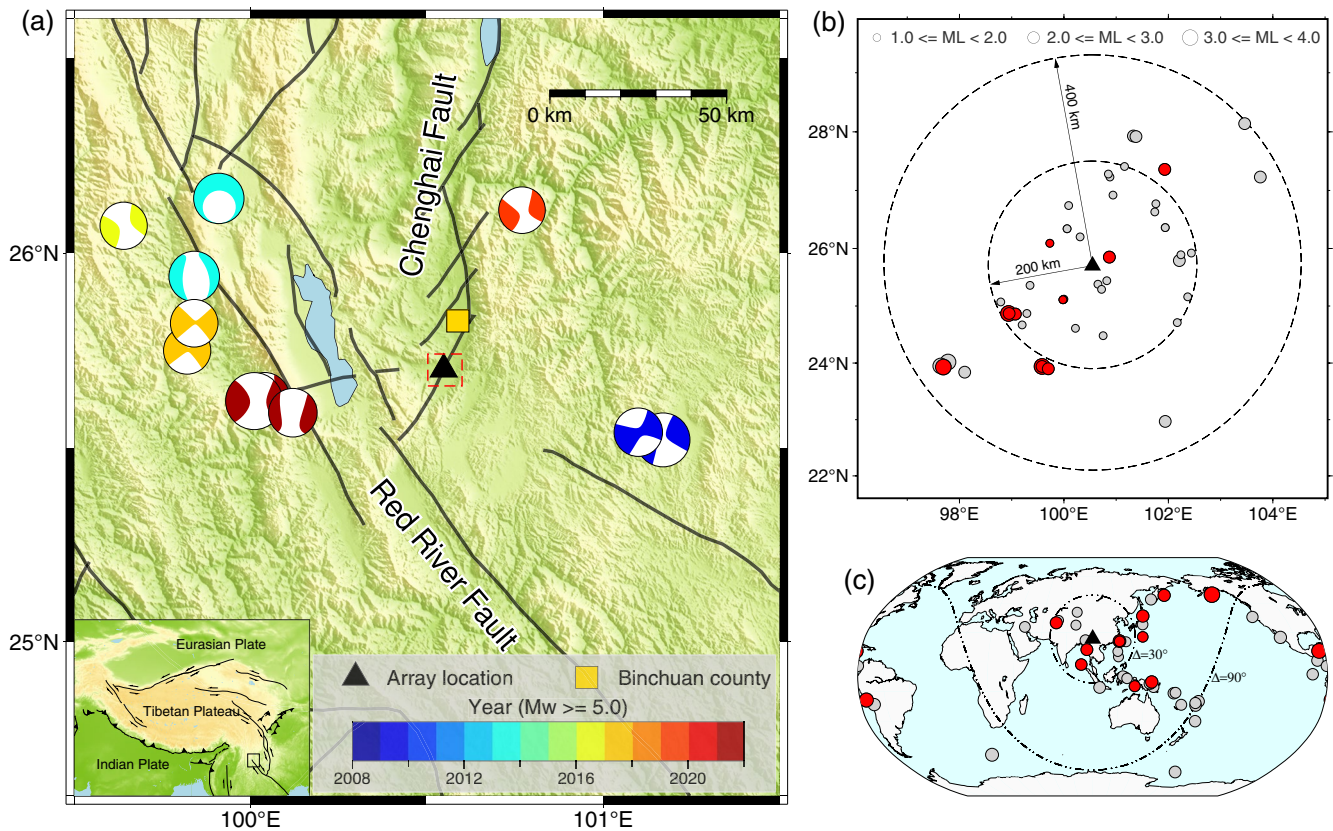
Figure 1. (a) Topographic map of Northwest Yunnan showing locations of regional faults (black lines), focal mechanisms of earthquakes with $M_W \geq 5$ since 2008 (colored beach balls), Binchuan County (yellow square), and the across-fault dense linear array used in this study (black triangle). Red dashed box represents the boundary of Figure 2. The inset map shows the Tibetan Plateau where the study region is marked by the black box. Major block boundary faults in western China (thinner black lines) and their types are obtained from the HimaTibetMap-1.1 database (Styron et al., 2010). (b) Spatial distribution of nearby earthquakes (circles) which occurred during deployment of dense array (black triangle). The events with epicentral distance larger than 200 km and $M_L < 2$ are not presented here. Red circles denote events recorded by the array with good signal-to-noise ratio (SNR). (c) Spatial distribution of the recorded teleseismic earthquakes (circles) and those having good SNR are indicated by red circles. Information about all earthquakes analyzed in this study are detailed in Table 1.

In this study, we systematically examine the variability of seismic site response across the Chenghai fault within the Binchuan basin using earthquake recordings from a dense linear array deployed in early 2018 (Yang et al., 2020). In the following sections, we first describe the tectonic setting of the study region, dense array configuration, and utilized seismic data. Then, we analyze the variations of peak ground velocity along the array using local earthquake recordings. From local, regional, and teleseismic earthquake recordings, we further apply the standard spectral ratio method to quantify the frequency-dependent amplifications caused by the subsurface structures and investigate their spatial pattern. In the end, we perform one-dimensional ground response analysis based on the shear-wave velocity (Vs) model derived from ambient noise tomography (Yang et al., 2020) and the transfer function method which assumes vertically propagating SH-waves from the bedrock. Our results reveal the significant amplification due to the near-surface low-velocity structures, and the considerable variability of seismic site response due to the strong lateral heterogeneities beneath the Binchuan basin.

2. Tectonic Setting and Data

2.1. Tectonic Setting

The Chenghai fault is an active northeast-trending, left-lateral fault in the southeastern margin of the Tibetan Plateau (Figure 1a) and has undergone strong and complex post-collision deformation. According to paleoseismic studies and modern seismological records, it has produced many moderate to large earthquakes including the 1515 M7.5 Yongsheng earthquake and the 2001 M6.0 Yongsheng earthquake (Luo et al., 2015). Along the ~200-km-long Chenghai fault zone, there exist several basins such as the Binchuan basin and Midu basin, which
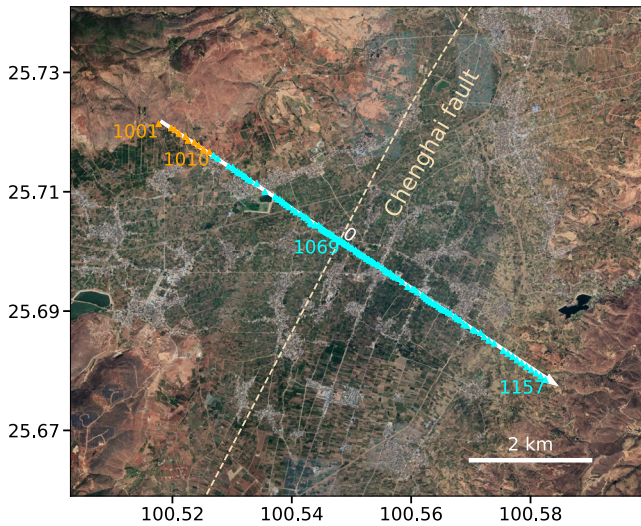
Figure 2. Layout of the dense linear array. Ten reference stations (from 1001 to 1010) are indicated by orange triangles and the remaining stations are marked by cyan triangles. Station 1069 is closest to the intersection point (named zero-offset) of the dense linear array and the mapped surface trace of the Chenghai fault (wheat dashed line) from Deng et al. (2003). The location of each station is hereafter denoted by the offset of its projection point along the white arrow, which is a linear fitting of the across-fault array.

are respectively controlled by the west-side-down and east-side-down normal displacement components on the fault (Wang et al., 1998). These Quaternary sedimentary basins would considerably enlarge the ground shaking level and cause severe damage to the buildings and facilities. For the Binchuan basin which has increasing infrastructures and population (~370,000 by 2021), its proximity to the intersection of the Chenghai and Red River faults, as well as frequent earthquakes nearby such as the 2021 Ms 6.4 Yangbi earthquake (e.g., Zhang et al., 2022), further increase the seismic hazard potential of this area (Figure 1a).

2.2. Dense Linear Array

In order to precisely monitor the subtle seismic velocity changes associated with high seismicity in western Yunnan, a transmitting seismic station (TSS) composed of a large-volume airgun array was first constructed in Binchuan in April 2011 (Wang et al., 2012). Subsequent cross-correlation analyses of waveforms recorded by surrounding permanent and portable stations indicated the potential temporal variations of subsurface structures near the southern section of the Chenghai fault (Liu et al., 2021; Luan et al., 2022; Yang et al., 2021). Consequently, between January 5 and February 7 in 2018, a temporary dense linear array consisting of 125 stations was deployed across the Chenghai fault zone in the south part of the Binchuan basin (Figure 2). Spanning the basin with an aperture of over 8 km from northwest to southeast, the linear array has the densest installation with an average interstation spacing of about 50 m near the mapped Chenghai fault trace. For the NW and SE portions, the average spacing is about 100 m. All the transportable seismic stations were equipped with the same intermediate-period (5 s) three-component sensor (EPS-2-M6Q) to record ground velocity at a sampling rate of 200 data points per second together with a GPS antenna to synchronize the clock.

2.3. Selection of Events and Time Windows

During the 1-month deployment period, a number of nearby earthquakes were detected by regional permanent stations and archived by the China Earthquake Data Center (Figure 1b). We first cut local earthquake waveforms out from continuous recordings across the array for events with local magnitude larger than 1.0 and epicentral distance less than 400 km. We exclude local earthquakes that are smaller than $M_L 2.0$ and more than 200 km far away from the array from further analyses because of their generally small amplitudes in seismograms. Then, we manually check the data quality of the remaining local earthquakes, and finally 11 out of them with a good signal-to-noise ratio (SNR) are selected (Figure 1b). The relatively small number of selected local earthquakes is because in the middle of the array, where most stations are adjacent to the residential areas and busy roads (Figure 2), the waveforms from some local events might be strongly contaminated by noise generated from human activities during the day.

To better analyze the time-frequency characteristics of recorded ground motions, we perform the sliding window Fast Fourier Transform with 60-s-long and 50% overlapping time windows on seismograms of the vertical component. At the most northwestern station 1001, a typical 24-hr spectrogram with lighter color representing higher power spectral density (PSD) during Julian day 14 and 15 in 2018 (Beijing Time) presents a consistently lower level of seismic noise and clear signals from both teleseismic and local earthquakes (Figure 3a). In comparison, the corresponding spectrogram at the zero-offset station 1069 shows stronger PSD between 1 and 10 Hz from 8 a.m. to 8 p.m (Figure 3b), indicating an obvious sub-daily variation pattern of cultural noise level, that is, activities generating strong seismic energies appear consistently during daytime but drop down significantly during nighttime. Moreover, we have observed persistent stronger PSD at a few certain frequencies (e.g., 0.4, 1.0, 2.0 Hz), suggesting that they are very likely caused by subsurface structures near the mapped fault trace instead of wind- or human-related activities (Figure 3b). We have also noticed that 10 out of 11 selected local earthquakes occurred during the night (Figure 3c), which are expected to produce more reliable results.
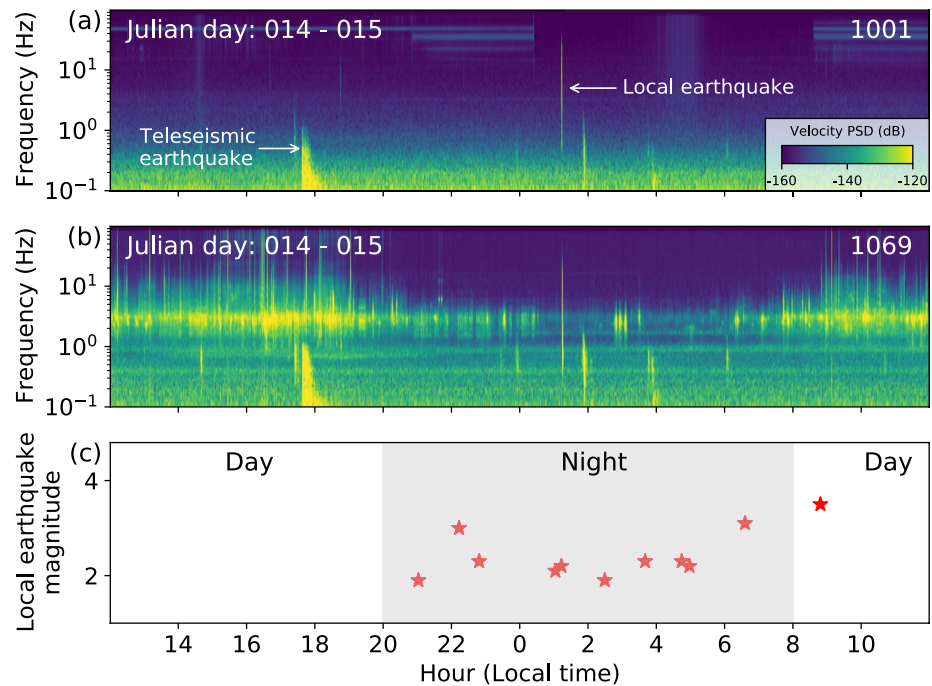
Figure 3. (a) A 24-hr spectrogram (power spectral density) of the vertical ground motions recorded at the most northwestern station (1001) on Julian day 14–15 in 2018. Note the different frequency contents of ground motions caused by teleseismic earthquakes (no more than 2 Hz) and local earthquakes (up to 50 Hz). (b) Similar to the uppermost panel, but at the zero-offset station (1069). (c) Temporal distribution of local earthquakes analyzed in this study and their corresponding local magnitudes.

In addition to waveforms of local earthquakes which appear as higher-energy bursts between ∼0.4 and ∼50 Hz in the spectrograms, seismic waves generated from teleseismic earthquakes consist of strong and more persistent lower-frequency energies below ∼2 Hz (Figures 3a and 3b) and could be utilized to investigate the site response related to deeper structures (Pratt et al., 2017). Since the instruments used here have a corner frequency of 0.2 Hz, we also take regional and teleseismic earthquakes into account to supplement and validate results from a limited number of local earthquakes. Waveforms of earthquakes with magnitudes larger than five are inspected. Out of all the distant events recorded by the array, 17 regional and teleseismic earthquakes with good SNR are eventually selected (Figure 1c). Detailed information about the selected events (28 in total) is given in Table 1.

The waveforms whose amplitudes are 1-2 orders of magnitude lower or greater than those of other waveforms from the same event are regarded as outliers (Figure S1 in Supporting Information S1). These anomalous earthquake recordings are probably caused by the malfunction of certain components. We have applied one method quantifying the difference in waveform amplitudes among earthquake recordings of each component to recognize all the anomalous waveforms (see Text S1 & Figure S2 in Supporting Information S1). For each selected event, stations that have recorded anomalous waveforms on any component will be removed without further analysis. Then, three-component waveforms of each earthquake at each station are detrended and tapered with a 5% hanning window. After removing the instrument response and bandpass-filtering with a wide frequency range (0.05-0.08-99-99.5 Hz), velocity waveforms are rotated from the ZNE (vertical, north, east) to the ZRT (vertical, radial, transverse) coordinate system.

In order to determine the time windows used for further analyses, we first apply the short-term-average/long-term-average (STA/LTA) method to the array recordings. Different STA/LTA parameters have been tested for selected earthquakes with varying epicentral distances and magnitudes (Figures S3, S4, S5 and S6 in Supporting Information S1). We find that 2s/60s is appropriate for local earthquakes, and 10s/120s works the best for regional and teleseismic earthquakes. Then for each earthquake, we average all STA/LTA curves in the vertical, radial, and transverse directions respectively. Based on the averaged three-component STA/LTA curves, P and S wave time windows are determined for all earthquakes, except for some teleseismic earthquakes whose S wave

Table 1
Selected Earthquakes

ID	Origin time	Longitude	Latitude	Depth	Magnitude
L1	2018-01-14 17:13:13	100.87	25.85	17	2.2
L2	2018-01-16 18:29:27	99.98	25.11	9	1.9
L3	2018-02-03 13:01:59	99.73	26.09	10	1.9
L4	2018-01-17 20:44:32	99.07	24.86	18	2.3
L5	2018-01-26 20:58:19	98.95	24.87	11	2.2
L6	2018-01-26 22:35:54	98.94	24.87	19	3.1
L7	2018-02-03 19:40:23	99.7	23.9	19	2.3
L8	2018-01-11 14:48:47	99.58	23.94	17	2.3
L9	2018-01-11 14:13:31	99.58	23.94	19	3
L10	2018-01-17 17:02:37	101.93	27.36	21	2.1
L11	2018-02-02 00:48:21	97.69	23.93	19	3.5
T1	2018-01-10 02:51:31	−83.5193	17.4743	10	7.5
T2	2018-01-11 18:26:24	96.0776	18.3629	9	6
T3	2018-01-14 09:18:45	−74.7095	−15.7589	39	7.1
T4	2018-01-14 09:19:29	70.7313	36.4525	199.53	5.3
T5	2018-01-18 17:48:39	132.8132	−6.3907	26.95	5.6
T6	2018-01-23 09:31:42	−149.073	56.0464	25	7.9
T7	2018-01-24 10:51:19	142.4323	41.1034	31	6.3
T8	2018-01-25 01:15:58	91.7802	8.2643	10	5.8
T9	2018-01-25 02:10:34	166.4464	55.5419	11.17	6.2
T10	2018-01-26 22:47:57	145.8477	−3.5138	10	6.3
T11	2018-01-31 07:07:00	70.8155	36.5432	191.19	6.1
T12	2018-02-04 13:12:51	121.7321	24.1787	10.15	5
T13	2018-02-04 13:56:41	121.7078	24.1572	12	6.1
T14	2018-02-05 20:56:22	140.1845	27.0011	467.22	5.3
T15	2018-02-06 15:50:43	121.658	24.1359	17	6.4
T16	2018-02-06 18:00:13	121.7764	24.1017	6.12	5.2
T17	2018-02-06 19:15:29	121.7516	23.9552	14	5.4

time windows are not recognizable from either the waveforms or mean STA/LTA curves. Although slight travel time differences (<1 s) across the array have been found from both local events (Yang et al., 2021) and teleseismic earthquakes (Yang et al., 2020), they are negligible in the present study because waveforms are analyzed within time windows of tens of seconds. One of the advantages of using this method is that the averaged STA/LTA curves could help enhance SNR and thus considerably reduce the picking uncertainties of S waves, especially for stations suffering from strong noise contamination or amplified coda of P waves. Detailed information about the selected time windows for all the selected earthquakes is given in Table S1 in Supporting Information S1.

Figure 4 shows the averaged STA/LTA curves and corresponding waveforms from an $M_L 3.1$ earthquake recorded by the array in both vertical and horizontal directions. Around and within the LVZ that was imaged by ambient noise tomography (Yang et al., 2020), the ground motions are significantly amplified and prolonged compared to recordings at both ends of the array, especially after S arrivals. As all waveforms are equally scaled, clearly we can observe that horizontal motions have a larger amplitude than vertical motions. Waveforms generated from other local, regional, and teleseismic earthquakes also reveal similar features of amplification and prolongation in the middle portion of the array (Figure S7 in Supporting Information S1).
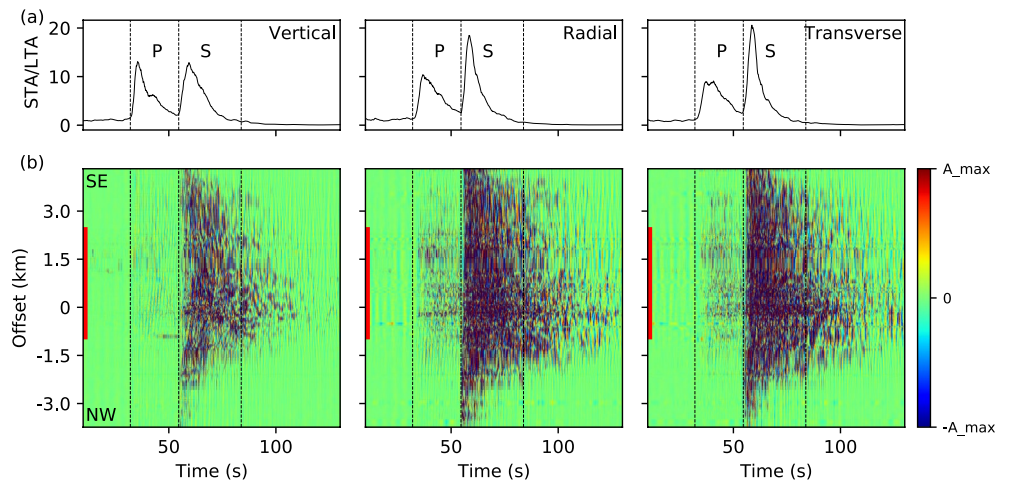
Figure 4. (a) The averaged short-term-average/long-term-average (STA/LTA) curves in the vertical, radial, and transverse directions for one local earthquake (Time: 2018-01-26 22:35:54, M_L: 3.1, Distance: 186.3 km), based on which P and S wave windows (black dashed lines) are determined for further analyses. (b) The corresponding array recordings that are bandpass-filtered from 0.1 to 50 Hz after removing anomalous traces. The waveforms are normalized by the largest vertical-component amplitude at station 1001 (A_max) and all traces along each *Y*-axis are sorted by their offsets. The low-velocity zone identified by Yang et al. (2020) is outlined by thick red lines. Details on anomalous traces and how they are discarded are included in the support information (Figure S1 and S2).

3. Analyses and Results

3.1. Peak Ground Velocity

The peak ground velocity (PGV), defined as the largest amplitude in the velocity seismogram, has been shown to correlate well with the macroseismic intensity, soil liquefaction potential, and earthquake damage to structures such as the buried pipelines (Akkar & Bommer, 2007). Although PGV could be estimated from empirical prediction equations, special caution should be taken when its spatial variability in a small region is appreciable (Johnson et al., 2020). The small-scale spatial changes of PGV values are often attributed to the heterogeneity near the surface, and in return, can be used to infer the lateral variation of subsurface structures.

We use the observed ground velocity waveforms from 11 selected local earthquakes to examine PGV and its spatial variability across the array. The waveforms are bandpass filtered between 0.1 and 50 Hz as seismic energies of recorded local earthquake waveforms largely fall into this frequency range. PGV values within the P and S wave time windows are respectively calculated for each waveform. The observed PGVs from these local earthquakes are generally consistent with the decaying log-log relationship of PGV with epicentral distance as predicted by the empirical ground motion prediction equation of Akkar and Bommer (2007) for S waves (Figure 5a). PGVs for P waves show a similar trend but overall have smaller values than those for S waves, and their results are included in Supporting Information S1 (Figure S8).

For each local event, we find that vertical PGVs are overall smaller than radial and transverse PGVs (as usually expected for local S waves). To study the PGV spatial variability across the array, for each component, we take the average of PGV values at 10 reference stations (from 1001 to 1010, Figure 2) as a reference and calculate the ratios of the observed PGVs to the reference PGV (PGV_ref). These ratios are later converted to logarithms of base 10 (Figure 5b). In general, both vertical and horizontal PGVs have larger values in the middle part of the array where an LVZ had been identified by both tomographic and receiver-function studies (Jiang et al., 2021; Yang et al., 2020). In addition, the spatial variability of horizontal PGVs is larger than that of vertical PGVs (Figure 5b). At the offset of −350 m (to the NW side of the fault trace), there exists a sharp increase of PGV in both radial and transverse directions, which may be related to a vertical boundary of shallow crustal materials. As the offset increases toward the southeast, PGVs gradually decrease and present relatively larger values than the northwestern part, which can be attributed to the relatively lower Vs at the southeastern part (Yang et al., 2020).

For different local events, we notice that the patterns of spatial variations of PGV are not identical. Sorting the events by their epicentral distances along the *Y*-axis, we observe that L1-L3, which have epicentral distances less
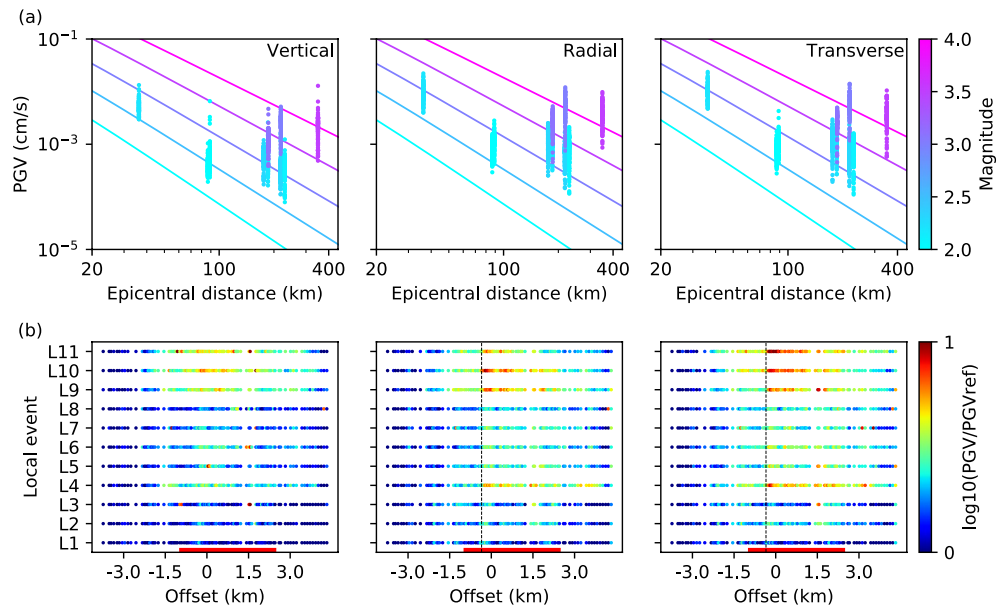
Figure 5. (a) Observed peak ground velocity (PGV) within the S wave window (colored dots) in the vertical, radial, and transverse directions for 11 local earthquakes as a function of both epicentral distance and magnitude. Solid lines show predicted PGV values based on the equation from Akkar and Bommer (2007). (b) Spatial variations of PGV within the S-wave window based on comparison between PGV at each station and the average PGV at reference stations (PGV$_{ref}$). Local events along the Y-axis are sorted by their epicentral distances from the array. The black dashed line marks the location of −350 m. Results of PGV within the P-wave window are included in the supporting information.

than 100 km, produce the least PGV spatial variability. L4-L8 with intermediate epicentral distances correspond to greater extents of PGV variations and L9-L11 with the largest epicentral distances have produced the most significant spatial variability in PGV (Figure 5b). To explain such changes among events and the relationship of PGV spatial variability with epicentral distance, the Fourier spectra of ground motions caused by the local event L1 with the minimum epicentral distance are calculated and explored (Figure 6). We find that, at station 1001, the spectral amplitudes of horizontal components are considerable from 10 to 20 Hz (note that the frequency axis is in the normal scale). This is attributed to the smaller source-receiver distance compared to other earthquakes, in which the higher-frequency seismic energies are less attenuated. While at another station 1069, due to the amplification and prolongation effects, the spectral amplitudes are much larger from 0.3 to 3 Hz, especially at ~1.5 Hz (Figure 6). But within the higher-frequency range (i.e., 10–20 Hz), the horizontal amplitudes are much

Figure 6. The smoothed Fourier spectra of horizontal ground velocity waveforms at station 1001 and 1069 generated from one local earthquake which has the smallest epicentral distance (Time: 2018-01-14 17:13:13, M$_L$: 2.2, Distance: 36.2 km).

smaller even though the source-receiver distance for station 1069 is slightly smaller, which should be caused by the strong local attenuation effects. Based on these observations, we thus conclude that the decreased PGV spatial variability for events with smaller epicentral distances results from the higher PGVs at the northwest side, which are attributed to the less attenuated high-frequency body waves. In other words, local earthquakes having larger epicentral distances tend to produce stronger spatial variability in PGV in our study area as evidenced in Figure 5b.
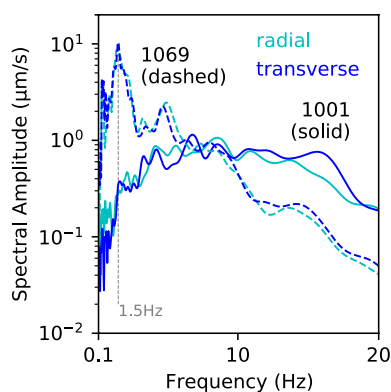
3.2. Standard Spectral Ratio

Direct amplitude measurements from earthquake recordings depend on the location and source properties of the earthquake and have difficulties in completely describing the effects of local geology (Borcherdt, 1970). In order to more precisely quantify the magnitude and corresponding frequency of amplification, here we apply the standard spectral ratio (SSR) method to the observed horizontal ground motions from local, regional, and teleseismic earthquakes. Only the recordings of horizontal components are used because

horizontal ground motions usually cause more damage and are affected by the local site conditions to a much larger extent than vertical ground motions. Similar to the applications of the SSR method in other regions (e.g., Pratt et al., 2017), the recordings of regional and teleseismic earthquakes are also analyzed to supplement and validate the observations derived from local earthquakes in this study. In addition, P and S waves of earthquakes are analyzed separately and seismic noises are also examined for any potential comparisons.

The SSR method requires a reference site (usually the bedrock site) at which the observed ground motions could be considered as the input motions for other nearby sites. Here we choose 10 stations at the northwest end of the array to be reference stations to eliminate the instability of a single reference site as with the PGV analysis. According to both geological (Wang et al., 1998) and tomographic (Yang et al., 2020) studies over the study region, these stations are located on the hard rock and their recordings are least affected by near-surface low-velocity layers. Though these stations are located on a hillside with a slight change in elevations (Figure 2), waveforms and spectra from earthquakes at these stations are inspected and are found to be similar to each other and have the same order of magnitude, suggesting that topographic effects have little influence on our results.

Waveforms within the analysis time windows (Table S1 in Supporting Information S1) are first detrended and tapered, after which we calculate their amplitude spectra from 0.1 to 10 Hz. The amplification phenomena typically appear within this frequency band (Figure 6), which is also of concern in engineering seismology. Next, all the initial Fourier spectra are smoothed using the Konno-Ohmachi method with a bandwidth coefficient of 40 as recommended by the SESAME (2004), which in most cases has the intermediate smoothing effect. Since spectra of horizontal components have almost the same shape and amplitude (Figure 6), they are further combined into one single spectrum by computing their geometric mean, termed as the horizontal spectrum. We calculate a reference horizontal spectrum ($U_{i,ref}(f)$) by taking the average of horizontal spectra at 10 reference stations (from 1001 to 1010):

$$U_{i,ref}(f) = \frac{1}{10} \cdot \sum_{k=1}^{10} \sqrt{R_{i,k} \cdot T_{i,k}} \tag{1}$$

Then spectral ratios across the array are calculated by:

$$SR_{i,j}(f) = \frac{U_{i,j}(f)}{U_{i,ref}(f)} \tag{2}$$

where $U_{i,j}(f)$ is the horizontal spectrum at station j for earthquake i, note that P and S waves of earthquakes are analyzed separately.

At each station, spectral ratios from P and S waves of 11 local earthquakes are averaged, and stations having less than six recorded earthquakes are removed to ensure reliability. Results from P waves are included in Supporting Information S1 since local P waves have relatively lower amplitude in the horizontal directions (Figure S9 in Supporting Information S1), and only observations from S waves are described below. High spectral ratios (>5) between 0.2 and 3 Hz have been observed in the middle part of the array, and much stronger amplification effects appear within the previously identified LVZ (Figure 7a). Around the fault trace (zero-offset), there exists a ~500-m-wide zone characterized by the highest amplification factors between ~0.4 and 2 Hz. As the selected local earthquakes have epicentral distances ranging from ~36 to ~350 km and various back azimuths, we also check the uncertainty by computing one standard deviation (STD) of all spectral ratios (Figure 7b). The uncertainty seems reasonable considering the aforementioned different locations and parameters of different sources.

At each station, spectral ratios from P and S waves of regional and teleseismic earthquakes are averaged between 0.1 and 2 Hz since their signals are mostly below 2 Hz and spectral ratios at higher frequencies would only reflect differences in terms of the background noise levels. We notice that the spectral ratio results from teleseismic P waves have shown a similar feature to those from S waves of local and teleseismic earthquakes (Figure 8). This is likely because teleseismic P waves contain P-to-S converted phases as well as their multiples, which originated from the shallow low-velocity layers beneath the array (Jiang et al., 2021).

To better and comprehensively describe the characteristics, we manually divide the array into four parts (Figure 8). The first part mostly contains the reference sites that are located on the hard rock, where no amplification of seismic waves are observed. The second part is near the west edge of the Binchuan basin, where the lower limit of the frequency band of amplification steadily decreases with the distance from the basin edge. We infer that the
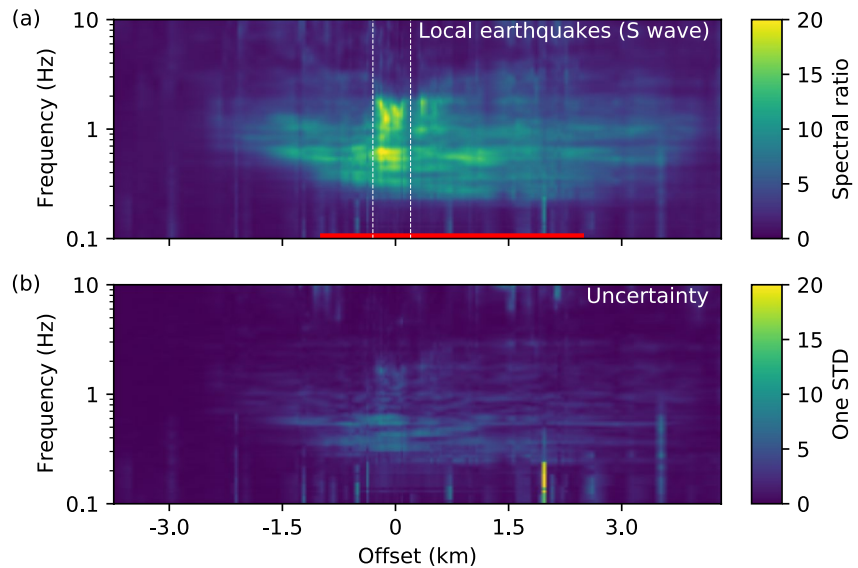
Figure 7. (a) The averaged spectral ratio results along the entire array obtained from S waves of local earthquakes. Two white dashed lines mark a 500-m wide zone around the fault. (b) The corresponding uncertainty.

basin thickness in this part might gradually increase toward the southeast considering that the deeper structure is more responsible for the amplification of lower frequency seismic waves. The third part is atop the middle of the Binchuan basin and around the mapped surface trace of the Chenghai fault, where spectral ratio results show large factors (up to 20) and extended frequency band (between 1 and 2 Hz) of amplification. Its width is about 500 m, and its northwest boundary coincides with the location where PGV values are observed to sharply increase. Based on these observations, we interpret that stronger local site effects within this segment are likely to be caused by a more localized low velocity zone embedded in the Binchuan basin which would act as a trapping structure. The fourth part has a longer length of about 4 km, where the amplification frequency band seems to be more persistent between 0.25 and 2 Hz. At the southeastern end of this part, the amplification factors of different frequencies generally decrease to one, suggesting no amplification (Figures 7 and 8).
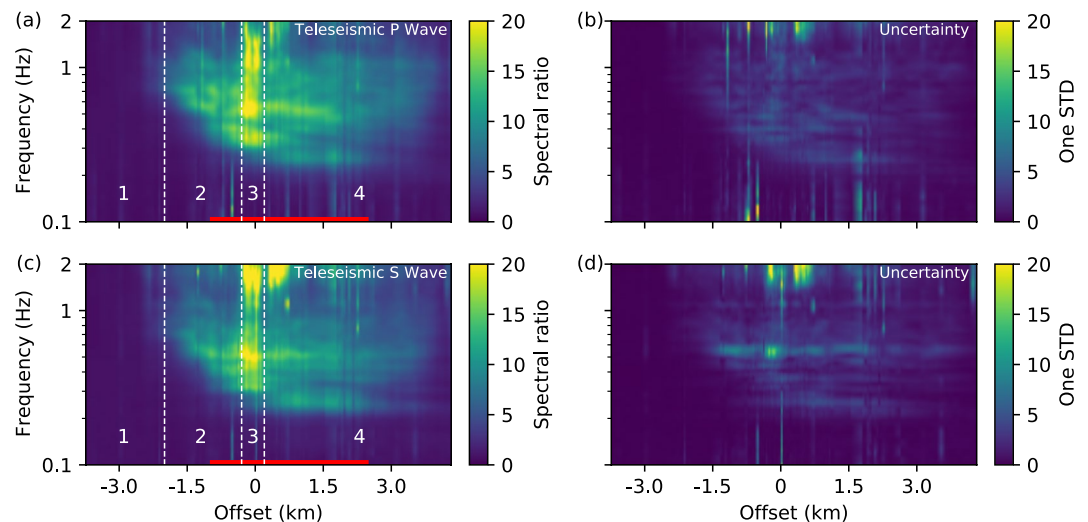

Figure 8. The averaged spectral ratio results along the entire array obtained from (a) P waves and (c) S waves of teleseismic earthquakes. The white dashed lines mark the boundaries between four parts that have different apparent features. The corresponding uncertainty results are in (b) and (d).
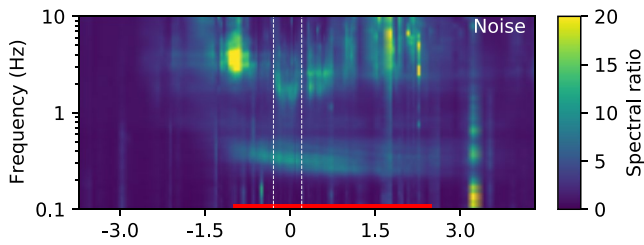
Figure 9. The averaged spectral ratio results along the entire array obtained from 120-s-long seismic ambient noise before P arrivals of local earthquakes.

LVZs have been observed to amplify not only seismic waves of earthquakes but also seismic ambient noise (e.g., Hillers et al., 2014; Nakamura, 1989). Our results have shown that different types of earthquake recordings would result in similar patterns of amplification in the space and frequency domain. In addition to earthquakes, it would be important to examine the amplification of seismic ambient noise. We choose 120 s time windows before the P arrivals of 11 local earthquakes for seismic noise. As we have demonstrated in Figure 3c, these recordings are expected to be less affected by noise from human activities. We apply the same procedure for the analysis of earthquake recordings to the selected noise data. The results show that noise levels within the previously identified LVZ are higher within the frequency band of 0.25–0.5 Hz, indicating that seismic noises are trapped there (Figure 9). However, the factors and frequency bands of amplification for ambient noise are much lower and narrower than those for earthquake recordings. Whether the third part would trap higher-frequency noise or not is unclear based on the results, which are significantly biased by cultural noises and have larger uncertainty (Figure S10 in Supporting Information S1).

3.3. SH-Wave Transfer Function

In this section, we aim to model the ground motion variations across the array based on the Vs model from Yang et al. (2020) and the transfer function method, which is widely used for ground response analysis. Based on the assumption that SH-waves propagate vertically from the underlying bedrock, the transfer function could be viewed as frequency-specific amplification or de-amplification of the input motion caused by the overlying mediums. The one-dimensional (1D) Vs profile under each station is first extracted from the Vs model through linear interpolation. Then the subsurface structure including Vs, Vp (compressional wave velocity), ρ (density), Qs (shear wave quality factor), and Qp (compressional wave quality factor) is derived using the empirical relationships among them (Brocher, 2005; Clouser & Langston, 1991; Dalton et al., 2009).

Transfer functions at all stations are computed using the Geopsy software (Wathelet et al., 2020), after which we also examine the modeled ground motion variations by applying the spectral ratio method to the calculated transfer functions. Given nearly identical 1D Vs models, transfer functions at reference stations are very similar to each other (Figures 10c and 10d). In comparison, low-velocity layers beneath station 1069 have resulted in
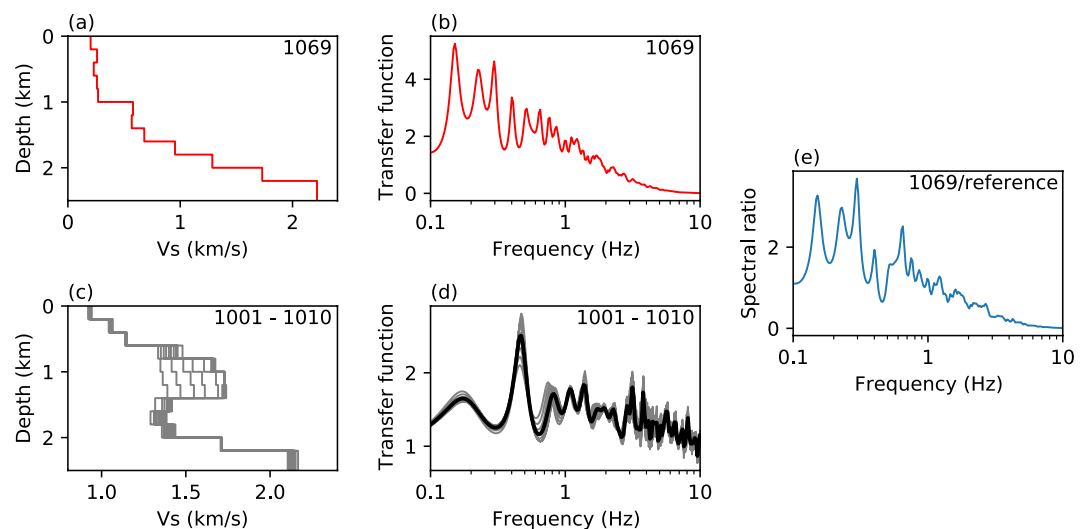

Figure 10. 1D shear wave velocity (Vs) profile interpolated from 2D Versus model (Figures 11a) in Yang et al. (2020) at (a) station 1069 and (c) reference stations (from 1001 to 1010). Transfer functions computed from 1D model at (b) station 1069 and (d) reference stations using Geopsy software developed by Wathelet et al. (2020). (e) Modeled spectral ratio results at station 1069 by dividing the red line in (b) by the black line in (d) which is the average of all transfer functions at reference stations.
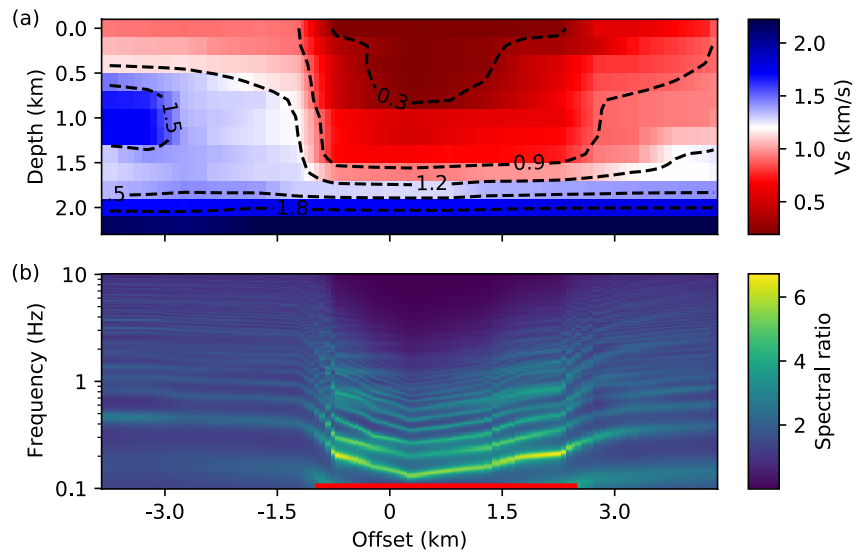
Figure 11. (a) The shear-wave velocity structure obtained from the ambient noise tomography (Yang et al., 2020). (b) Calculated spectral ratios between all transfer functions and the reference transfer function.

amplification and reverberations of SH-waves and therefore higher transfer function values at certain frequencies (Figures 10a and 10b). Again we take the average of transfer functions at 10 reference stations (from 1001 to 1010) as a reference, and spectral ratios of the transfer function at one station to the reference transfer function could be regarded as the frequency-dependent ground motion variations (Figure 10e).

Figure 11 shows the modeled spectral ratio result along the array based on the Vs model from Yang et al. (2020), from which we find that spectral ratios are higher below 1 Hz but are much lower above 1 Hz within the LVZ. As lower Vs usually corresponds to lower Q (i.e., stronger attenuation), the amplitude of higher-frequency waves would decrease considerably due to frequency-dependent attenuation. As the input (inverted) Vs model has a uniform grid size of 200 m in the depth direction and lacks sensitivity to the practical interfaces of impedance contrast, the modeled result contains some stripes of high spectral ratios. Compared to the observed spectral ratios of earthquake recordings, the amplification factors calculated from the simple transfer function modeling are underestimated. To solve such kinds of problems, it is important to derive higher resolution subsurface structures to better constrain depths and lateral variations of impedance interfaces, and to perform 2D or 3D forward modeling to obtain more accurate predictions.

Transfer functions represent differences between the input motions and ground surface motions. Note that deeper structures of the utilized Versus model are nearly identical (Figures 11a), thus differences between transfer functions at two stations result from different shallower structures beneath them. Therefore, amplification factors calculated from either practical earthquake recordings or theoretical transfer functions represent magnitudes of amplification compared to the reference ground motion. Since in most cases the input motions at depth are smaller than the actual reference ground motion, the amplification factors might be inevitably underestimated.

4. Discussion

4.1. Subsurface Structure Revealed by Dense Array Observations

The Chenghai fault zone has varying earthquake activity levels at different segments, for example, relatively weaker seismicity in Binchuan basin compared to other portions. Being a fault subsidence basin as suggested by many geological studies (e.g., Luo et al., 2015; Wang et al., 1998), the Binchuan basin holds the key to understanding the evolution process of the Chenghai fault zone and its surrounding region. Therefore, it is important to better constrain the basin structures including the basin edge and bedrock depth. In the previous section, we have shown clear site-to-site variabilities in seismic site response revealed by our dense array deployed in the Binchuan basin. Benefiting from the short interstation spacings (~50 m), we could delineate the subsurface structure beneath our array directly based on different types of observations.

PGV results of horizontal components clearly show a sharp increase at the offset −350 m (Figure 5b), which is also presented in the SSR results (Figure 7a). We suggest that this is likely caused by a nearly vertical interface separating two blocks of subsurface materials. To validate our speculation, we further compare our observations with the existing tomographic and geological results. We find that this newly found boundary corresponds to the west edge of an LVZ bounded by the 0.3 km/s isoline in the tomographic Vs model (Figures 11a), which also indicates that horizontal ground motions are significantly influenced by the shallower structures in this region. Furthermore, according to an adjacent geological profile with similar NW-SE orientation to our array (Luo et al., 2015), basin materials in our study area consist primarily of Quaternary sediments but show lateral variations in terms of sedimentary deposit types. Thus the boundary might be related to the abrupt changes of deposit materials, and the stronger amplification effects in the middle of Binchuan basin are attributed to unconsolidated deposits with lower shear-wave velocity.

Near the northwest edge of LVZ, the lower limit of the amplification frequency band of observed spectral ratio results gradually increase with the distance from the basin center (Figures 7a, 8a,). If assuming the shear wave velocity (V_s) in this part is constant, the primary resonance peak frequency (F_0) would decrease with the increasing thickness of low-velocity layer (h) based on the quarter-wavelength approximation:

$$F_0 = V_s/4h \tag{3}$$

Therefore, the thickness of sediments may gradually increase toward the southeast till the above-mentioned abrupt vertical interface. Such interpretation is consistent with the west-side down normal faulting on the fault plane. Besides, the Quaternary sedimentary isobath map of Binchuan area also indicates the bedrock depth at the northwest flank has a more gentle slope than that at another side (Luo et al., 2015).

In the very shallow crust of the Binchuan region, strong lateral heterogeneity has been observed to cause complex seismic wave propagation characteristics using airgun-generated P waves and a dense seismic array (She et al., 2019). Similarly, incoming seismic waves produced by earthquakes would not only be affected by the material contrasts in the vertical direction but also strongly affected by lateral structural variations. For example, a basement with varying depths would focus or defocus seismic waves and a low velocity fault zone would act as a waveguide to produce trapped waves with resonance modes (e.g., Qiu et al., 2020; Zhu et al., 2015). To better explain the observed variations in different kinds of ground motion, subsurface structures (e.g., velocity and quality factor) with higher resolution in both vertical and lateral directions are essential.

At some stations inside the basin, for example, stations between 1,000 m and 2,000 m, the lower limits of the amplification frequency bands are at ∼0.2 Hz. However, because the corner frequency of our instruments is 0.2 Hz, the potential amplification at longer periods might not be captured by this array and demands future analysis based on broadband seismometers in this region. In future studies, to more reliably resolve the subsurface structures such as the depth of horizontal impedance or the location of vertical impedance, joint inversion from different observations such as dispersion curves and HVSR would be helpful.

4.2. An Effective Method to Delineate Fault Zone

Large continental faults have hierarchical damage zones at shallow depths, forming narrow tabular or wedge-shaped LVZs near the main slip interfaces (e.g., Ben-Zion & Sammis, 2003; Wang et al., 2019; Yang, 2015). The width of fault damage zones usually ranges from tens of meters to several hundred meters and increases with the cumulative displacement of the fault (Faulkner et al., 2011). Along the Chenghai fault in northwest Yunnan, Yang et al. (2020) observed a ∼3.5-km-wide LVZ with delay time analysis of teleseismic arrivals and ambient noise tomography, which was later interpreted as sediments in the Binchuan basin. In this study, using seismograms recorded by the same dense linear array, we further analyze local site effects related to the Chenghai fault zone as well as their spatial variabilities. As expected, ground motions caused by both local and teleseismic earthquakes are significantly amplified across the wide LVZ previously found by Yang et al. (2020). Within the LVZ, we find a more localized zone of ∼500 m wide around the fault surface trace where ground motions are further amplified between ∼0.4 and 2 Hz (Figure 7a). As mentioned in Section 3.2, the subsurface medium in such a narrower zone may have lower wave speed and could act as a trapping structure to amplify arriving seismic waves. Considering the surface trace of the Chenghai fault intersects with our array exactly within this zone, it may correspond to the fault damage zone.

Delay time analysis of teleseismic arrivals could provide velocity lateral variations beneath the dense array, but it largely suffers from uncertainties of phase picking such as larger uncertainties for less impulsive S wave arrivals. Although tomographic method based on ambient noise had been used to image finer-scale subsurface structures, results with a horizontal resolution of a few hundred meters still have difficulties in capturing the small-scale fault damage zone. Site-to-site variability of seismic response based on observed waveforms could help better constrain the lateral variations of subsurface structures with higher resolution and more reliability. For example, the energy of fault zone trapped waves below 3 Hz has been observed in strong agreement with the fault damage zone structures of the Clark fault in California, especially with respect to the width (e.g., Wang et al., 2019). Our seismic site response results present the most strongly amplified seismic waves below 2 Hz in a ∼500-m-wide zone around the Chenghai fault, which may be associated with the fault damage zone. Since this smaller-scale fault zone structure was not clearly identified through either delay time analysis of teleseismic arrivals or ambient noise tomography, we suggest that analyzing site response across a dense array can be an effective method to identify fault zones when geological settings are complicated.

However, to verify whether the 500-m-wide zone is indeed a fault damage zone, a near vertical conduit extending along the fault interface, or a shallow localized structure, demands further analysis. Since the strong impedance at the basin basement could produce seismic waves with longer periods and larger amplitudes, higher-frequency waves trapped by shallower low velocity fault zone may have been obscured in the time series. For this reason, such trapped waves would be difficult to be detected if directly applying the typical features of fault zone trapped/guided waves (Ross & Ben-Zion, 2015). Indeed, fault zone trapped waves are not identified at stations within the 500-m zone in teleseismic earthquake waveforms (Yang et al., 2020). Because the number of near-fault local earthquakes during the deployment time window was limited, systematic analysis of waveforms in a typical frequency band of fault zone trapped waves (2–6 Hz) is not available. High-frequency noise tomography could be used to improve the resolution of shallow structures to distinguish the possibility of a localized near-surface trapping structure. It is beyond the scope here and will be conducted in future studies because the array crossed several roads in the region, and thus a careful analysis of the noise source has to be performed before a reliable shallow velocity structure can be derived.

4.3. Implications for Future Microzonation

The small-scale variations of site response have long been observed (e.g., Borcherdt, 1970; Gutenberg, 1957; Hough et al., 1990), but have not been comprehensively investigated until recent decades with the growing deployments of dense seismic arrays (e.g., Johnson et al., 2020; Steidl, 1993; Thomas et al., 2020). The latest dense array observations underscore the strong effects of shallow crust on the ground motion at rather a small scale (Johnson et al., 2020) as well as the feasibility of imaging the shallow subsurface structure by inverting the HVSR curve together with some prior information (Thomas et al., 2020). In this study, the dense linear array equipped with three-component geophones provides an unprecedented opportunity to estimate the seismic site response in Binchuan region, northwestern Yunnan at a very high resolution (tens of meters). In addition to our linear array, a two-dimensional array was deployed with ∼2 km spacing that covered the entire Binchuan basin (e.g., Jiang et al., 2020). Such analyses can be certainly conducted in the 2D array to map out along-strike variation of site responses near the Chenghai fault.

As the instruments are all-in-one units and can be easily deployed, they may be applied in urban areas for microzonation, complementing shallow borehole measurements. On the other hand, with the rapid development of an unconventional and ultra-dense seismic array: distributed acoustic sensing (DAS) system, massive site investigation in an urban area has become possible (e.g., Spica et al., 2020). Recently, a DAS experiment based on repeatable large-volume airgun source and internet fiber has been conducted in the populated Binchuan county (Song et al., 2021), which demonstrates its potential applications in subsurface medium monitoring as well as urban microzonation.

5. Conclusions

In this study, we analyze the seismic site response across the Chenghai fault based on a dense linear array equipped with three-component instruments. We observe clear spatial variations in PGV of local earthquakes across the array with larger values in the middle part and find the variability is more prominent in the horizontal directions.

After sorting local events by their epicentral distances, we notice that events having larger source-receiver distances tend to produce larger variability of PGV, which can be attributed to the frequency-specific modifications of subsurface structures beneath the array to the arriving seismic waves. Combining with regional and teleseismic P and S waves, we further examine the relative ground motions between 0.1 and 10 Hz through the SSR method. Results from different types of earthquakes and waveforms are overall consistent with each other, and 0.2–2 Hz horizontal ground motions inside the basin are significantly amplified by factors up to 20. Because of the short interstation spacing (tens of meters), we discover a more localized trapping structure (∼500 m) surrounding the fault surface trace and the variations of frequency-dependent amplification across the array generally correlate well with lateral changes of subsurface structures. As imaging the shallow crust based on the dense seismic array is becoming more and more popular, inspecting the seismic site response, as well as its spatial variability, is expected to provide important constraints on the subsurface structures.

Data Availability Statement

Waveform data used in this study are available in figshare (https://doi.org/10.6084/m9.figshare.14898327.v1) and Data Management Centre of China Seismic Experimental Site (http://www.cses.ac.cn). Figure 1 is plotted with GMT 6 (Wessel et al., 2019) and other figures are plotted with Matplotlib (Hunter, 2007).

References

Akkar, S., & Bommer, J. J. (2007). Empirical prediction equations for peak ground velocity derived from strong-motion records from Europe and the Middle East. *Bulletin of the Seismological Society of America*, *97*(2), 511–530.

Beck, J. L., & Hall, J. F. (1986). Factors contributing to the catastrophe in Mexico City during the earthquake of September 19, 1985. *Geophysical Research Letters*, *13*(6), 593–596.

Ben-Zion, Y., & Aki, K. (1990). Seismic radiation from an SH line source in a laterally heterogeneous planar fault zone. *Bulletin of the Seismological Society of America*, *80*(4), 971–994.

Ben-Zion, Y., & Sammis, C. G. (2003). Characterization of fault zones. *Pure and Applied Geophysics*, *160*(3), 677–715.

Ben-Zion, Y., Vernon, F. L., Ozakin, Y., Zigone, D., Ross, Z. E., Meng, H., et al. (2015). Basic data features and results from a spatially dense seismic array on the San Jacinto fault zone. *Geophysical Journal International*, *202*(1), 370–380.

Borcherdt, R. D. (1970). Effects of local geology on ground motion near San Francisco Bay. *Bulletin of the Seismological Society of America*, *60*(1), 29–61.

Brocher, T. M. (2005). Empirical relations between elastic wavespeeds and density in the Earth's crust. *Bulletin of the Seismological Society of America*, *95*(6), 2081–2092.

Chen, X., & Yang, H. (2020). Effects of seismogenic width and low-velocity zones on estimating slip-weakening distance from near-fault ground deformation. *Geophysical Journal International*, *223*(3), 1497–1510.

Clouser, R. H., & Langston, C. A. (1991). Qp-Qs relations in a sedimentary basin using converted phases. *Bulletin of the Seismological Society of America*, *81*(3), 733–750.

Cox, B. R., Cheng, T., Vantassel, J. P., & Manuel, L. (2020). A statistical representation and frequency-domain window-rejection algorithm for single-station HVSR measurements. *Geophysical Journal International*, *221*(3), 2170–2183.

Dalton, C. A., Ekström, G., & Dziewonski, A. M. (2009). Global seismological shear velocity and attenuation: A comparison with experimental observations. *Earth and Planetary Science Letters*, *284*(1–2), 65–75.

Day, S. M., Graves, R., Bielak, J., Dreger, D., Larsen, S., Olsen, K. B., et al. (2008). Model for basin effects on long-period response spectra in southern California. *Earthquake Spectra*, *24*(1), 257–277.

Deng, Q. D., Zhang, P. Z., Ran, Y. K., Yang, X. P., Min, W., & Chen, L. C. (2003). Active tectonics and earthquake activities in China. *Earth Science Frontiers*, *10*(S1), 66–73. https://doi.org/10.1007/s12583-020-1321-y

Dunham, E. M., & Bhat, H. S. (2008). Attenuation of radiated ground motion and stresses from three-dimensional supershear ruptures. *Journal of Geophysical Research: Solid Earth*, *113*(B8).

Faulkner, D., Mitchell, T., Jensen, E., & Cembrano, J. (2011). Scaling of fault damage zones with displacement and the implications for fault growth processes. *Journal of Geophysical Research: Solid Earth*, *116*(B5).

Frankel, A., Stephenson, W., & Carver, D. (2009). Sedimentary basin effects in Seattle, Washington: Ground-motion observations and 3D simulations. *Bulletin of the Seismological Society of America*, *99*(3), 1579–1611.

Gutenberg, B. (1927). *Grundlagen der erdbebenkunde* (Vol. 12). Gebrüder Borntraeger.

Gutenberg, B. (1957). Effects of ground on earthquake motion. *Bulletin of the Seismological Society of America*, *47*(3), 221–250.

Hassani, B., & Atkinson, G. M. (2016). Applicability of the site fundamental frequency as a VS 30 proxy for central and eastern North America. *Bulletin of the Seismological Society of America*, *106*(2), 653–664.

Hillers, G., Campillo, M., Ben-Zion, Y., & Roux, P. (2014). Seismic fault zone trapped noise. *Journal of Geophysical Research: Solid Earth*, *119*, 5786–5799. https://doi.org/10.1002/2014JB011217

Hough, S. E., Friberg, P., Busby, R., Field, E., Jacob, K., & Borcherdt, R. (1990). Sediment-induced amplification and the collapse of the Nimitz Freeway. *Nature*, *344*(6269), 853–855.

Huang, Y., Li, H., Liu, X., Zhang, Y., Liu, M., Guan, Y., et al. (2020). The multiscale structure of the Longmen Shan central fault zone from local and teleseismic data recorded by short-period dense arrays. *Bulletin of the Seismological Society of America*, *110*(6), 3077–3087.

Hunter, J. D. (2007). Matplotlib: A 2D graphics environment. *IEEE Annals of the History of Computing*, *9*(03), 90–95.

Jiang, X., Hu, S., & Yang, H. (2021). Depth extent and Vp/Vs ratio of the Chenghai fault zone, Yunnan, China constrained from dense-array-based teleseismic receiver functions. *Journal of Geophysical Research: Solid Earth*, *126*, e2021JB022190. https://doi.org/10.1029/2021JB022190

Jiang, X., Yang, H., Yang, W., & Wang, W. (2020). Crustal structure in the Binchuan basin of Yunnan constrained from receiver functions on a 2-D seismic dense array. *Earthquake Science*, *33*, 264–272. https://doi.org/10.29382/eqs-2020-0264-01

Johnson, C. W., Kilb, D., Baltay, A., & Vernon, F. (2020). Peak ground velocity spatial variability revealed by dense seismic array in southern California. *Journal of Geophysical Research: Solid Earth*, *125*(6), e2019JB019157.

Kawase, H. (2003). Site effects on strong ground motions. *International Geophysics Series*, *81*(B), 1013–1030.

Kurzon, I., Vernon, F. L., Ben-Zion, Y., & Atkinson, G. (2014). Ground motion prediction equations in the San Jacinto fault zone: Significant effects of rupture directivity and fault zone amplification. *Pure and Applied Geophysics*, *171*(11), 3045–3081.

Lewis, M., Peng, Z., Ben-Zion, Y., & Vernon, F. (2005). Shallow seismic trapping structure in the San Jacinto fault zone near Anza, California. *Geophysical Journal International*, *162*(3), 867–881.

Li, Y. G., & Vernon, F. L. (2001). Characterization of the San Jacinto fault zone near Anza, California, by fault zone trapped waves. *Journal of Geophysical Research: Solid Earth*, *106*(B12), 30671–30688.

Lin, F.-C., Li, D., Clayton, R. W., & Hollis, D. (2013). High-resolution 3D shallow crustal structure in Long Beach, California: Application of ambient noise tomography on a dense seismic array. *Geophysics*, *78*(4), Q45–Q56.

Liu, C., Yang, H., Wang, B., & Yang, J. (2021). Impacts of reservoir water level fluctuation on measuring seasonal seismic travel time changes in the Binchuan basin, Yunnan, China. *Remote Sensing*, *13*(12), 2421. https://doi.org/10.3390/rs13122421

Luan, Y., Yang, H., Wang, B., Yang, W., Wang, W., Yang, J., et al. (2022). Time-lapse monitoring of daily velocity changes in Binchuan, south-western China, using large-volume air-gun source array data. *Seismological Research Letters*. https://doi.org/10.1785/0220210160

Luo, R.-J., Wu, Z.-H., Huang, X.-l., Zhou, C., & Tian, T. (2015). The main active faults and the active tectonic system of Binchuan area, north-western Yunnan. *Geological Bulletin of China*, *34*(1), 155–170.

Milne, J., (1908). *Seismology* (Vol. 85): K. Paul Trench Trubner.

Murphy, J., Davis, A., & Weaver, N. (1971). Amplification of seismic body waves by low-velocity surface layers. *Bulletin of the Seismological Society of America*, *61*(1), 109–145.

Nakamura, Y. (1989). A method for dynamic characteristics estimation of subsurface using microtremor on the ground surface. Railway Technical Research Institute. *Quarterly Reports*, *30*(1).

Nakamura, Y. (2019). What is the Nakamura method? *Seismological Research Letters*, *90*(4), 1437–1443.

Ni, S., Kanamori, H., & Helmberger, D. (2005). Energy radiation from the Sumatra earthquake. *Nature*, *434*(7033), 582.

Olsen, K. (2000). Site amplification in the Los Angeles basin from three-dimensional modeling of ground motion. *Bulletin of the Seismological Society of America*, *90*(6B), S77–S94.

Pratt, T. L., Brocher, T. M., Weaver, C. S., Creager, K. C., Snelson, C. M., Crosson, R. S., et al. (2003). Amplification of seismic waves by the Seattle basin, Washington State. *Bulletin of the Seismological Society of America*, *93*(2), 533–545.

Pratt, T. L., Horton, J. W., Jr, Muñoz, J., Hough, S. E., Chapman, M. C., & Olgun, C. G. (2017). Amplification of earthquake ground motions in Washington, DC, and implications for hazard assessments in central and eastern North America. *Geophysical Research Letters*, *44*(24), 12150–112160.

Qiu, H., Allam, A. A., Lin, F. C., & Ben-Zion, Y. (2020). Analysis of fault zone resonance modes recorded by a dense seismic array across the san Jacinto fault zone at Blackburn Saddle. *Journal of Geophysical Research: Solid Earth*, *125*(10),e2020JB019756.

Qiu, H., Ben-Zion, Y., Catchings, R., Goldman, M. R., Allam, A. A., & Steidl, J. (2021). Seismic imaging of the Mw 7.1 Ridgecrest earthquake rupture zone from data recorded by dense linear arrays. *Journal of Geophysical Research: Solid Earth*, *126*, e2021JB022043. https://doi.org/10.1029/2021JB022043

Reid, H. F. (1910). *The California earthquake of April 18, 1906: The Mechanics of the earthquake/by Harry Fielding Reid*. Carnegie Institute.

Ross, Z. E., & Ben-Zion, Y. (2015). An algorithm for automated identification of fault zone trapped waves. *Geophysical Journal International*, *202*(2), 933–942.

Roux, P., Moreau, L., Lecointre, A., Hillers, G., Campillo, M., Ben-Zion, Y., et al. (2016). A methodological approach towards high-resolution surface wave imaging of the San Jacinto Fault Zone using ambient-noise recordings at a spatially dense array. *Geophysical Journal International*, *206*(2), 980–992.

Rovelli, A., Caserta, A., Marra, F., & Ruggiero, V. (2002). Can seismic waves be trapped inside an inactive fault zone? The case study of Nocera Umbra, central Italy. *Bulletin of the Seismological Society of America*, *92*(6), 2217–2232.

Sahakian, V. J., Baltay, A., Hanks, T. C., Buehler, J., Vernon, F., Kilb, D., et al. (2019). Ground motion residuals, path effects, and crustal properties: A pilot study in southern California. *Journal of Geophysical Research: Solid Earth*, *124*(6), 5738–5753.

SESAME. (2004). *Guidelines for the implementation of the H/V spectral ratio technique on ambient vibrations: Measurements, processing, and interpretations. SESAME European Research Project WP12—D23.12.*

Share, P.-E., Tábořík, P., Štěpančíková, P., Stemberk, J., Rockwell, T. K., Wade, A., et al. (2020). Characterizing the uppermost 100 m structure of the San Jacinto fault zone southeast of Anza, California, through joint analysis of geological, topographic, seismic and resistivity data. *Geophysical Journal International*, *222*(2), 781–794.

She, Y., Yao, H., Wang, W., & Liu, B. (2019). Characteristics of seismic wave propagation in the Binchuan region of Yunnan using a dense seismic array and large volume airgun shots. *Earthquake Research in China*, *33*(2), 174–185.

Singh, S., Pacheco, J., García, D., & Iglesias, A. (2006). An estimate of shear-wave Q of the mantle wedge in Mexico. *Bulletin of the Seismological Society of America*, *96*(1), 176–187.

Somerville, P. G., Smith, N. F., Graves, R. W., & Abrahamson, N. A. (1997). Modification of empirical strong ground motion attenuation relations to include the amplitude and duration effects of rupture directivity. *Seismological Research Letters*, *68*(1), 199–222.

Song, Z., Zeng, X., Wang, B., Yang, J., Li, X., & Wang, H. F. (2021). Distributed acoustic sensing using a large-volume Airgun source and internet fiber in an urban area. *Seismological Research Letters*, *92*(3), 1950–1960.

Spica, Z. J., Perton, M., Martin, E. R., Beroza, G. C., & Biondi, B. (2020). Urban seismic site characterization by fiber-optic seismology. *Journal of Geophysical Research: Solid Earth*, *125*(3), e2019JB018656.

Steidl, J. H. (1993). Variation of site response at the UCSB dense array of portable accelerometers. *Earthquake Spectra*, *9*(2), 289–302.

Steidl, J. H., Tumarkin, A. G., & Archuleta, R. J. (1996). What is a reference site? *Bulletin of the Seismological Society of America*, *86*(6), 1733–1748.

Styron, R., Taylor, M., & Okoronkwo, K. (2010). Database of active structures from the Indo-Asian collision. *Eos, Transactions American Geophysical Union*, *91*(20), 181–182.

Thomas, A. M., Spica, Z., Bodmer, M., Schulz, W. H., & Roering, J. J. (2020). Using a dense seismic array to determine structure and site effects of the two towers earthflow in northern California. *Seismological Research Letters*, *91*(2A), 913–920.

Wang, B., Ge, H., Yang, W., Wang, W., Wang, B., Wu, G., et al. (2012). Transmitting seismic station monitors fault zone at depth. *Eos, Transactions American Geophysical Union*, *93*(5), 49–50.

Wang, E., Burchfiel, B., Royden, L., Liangzhong, C., Jishen, C., Wenxin, L., et al. (1998). *Late Cenozoic Xianshuihe-Xiaojiang, Red River, and Dali Fault Systems of Southwestern Sichuan and Central Yunnan, China* (Vol. 327, pp. 1–108). Special Paper-Geological Society of America.

Wang, Y., Allam, A., & Lin, F. C. (2019). Imaging the fault damage zone of the San Jacinto Fault near Anza with ambient noise tomography using a dense nodal array. *Geophysical Research Letters*, *46*(22), 12938–12948.

Wathelet, M., Chatelain, J. L., Cornou, C., Giulio, G. D., Guillier, B., Ohrnberger, M., et al. (2020). Geopsy: A user-friendly open-source tool set for ambient vibration processing. *Seismological Research Letters*, *91*(3), 1878–1889.

Weng, H., Yang, H., Zhang, Z., & Chen, X. (2016). Earthquake rupture extents and coseismic slips promoted by damaged fault zones. *Journal of Geophysical Research: Solid Earth*, *121*(6), 4446–4457.

Wessel, P., Luis, J. F., Uieda, L., Scharroo, R., Wobbe, F., Smith, W. H. F., et al. (2019). The generic mapping tools version 6. *Geochemistry, Geophysics, Geosystems*, *20*(11), 5556–5564.

Wirth, E. A., Vidale, J. E., Frankel, A. D., Pratt, T. L., Marafi, N. A., Thompson, M., et al. (2019). Source-dependent amplification of earthquake ground motions in deep sedimentary basins. *Geophysical Research Letters*, *46*(12), 6443–6450.

Wu, C., Peng, Z., & Ben-Zion, Y. (2009). Non-linearity and temporal changes of fault zone site response associated with strong ground motion. *Geophysical Journal International*, *176*(1), 265–278.

Yang, H. (2015). Recent advances in imaging crustal fault zones: A review. *Earthquake Science*, *28*(2), 151–162.

Yang, H., Duan, Y., Song, J., Jiang, X., Tian, X., Yang, W., et al. (2020). Fine structure of the Chenghai fault zone, Yunnan, China, constrained from teleseismic Travel time and ambient noise tomography. *Journal of Geophysical Research: Solid Earth*, *125*(7),e2020JB019565.

Yang, H., Duan, Y., Song, J., Yang, W., Wang, W., Tian, X., et al. (2021). Illuminating high-resolution crustal fault zones and temporal changes using multi-scale dense arrays and airgun sources. *Earthquake Research Advances*, *1*(1), 100001. https://doi.org/10.19743/j.cnki.0891-4176.202101002

Yang, H., Li, Z., Peng, Z., Ben-Zion, Y., & Vernon, F. (2014). Low-velocity zones along the San Jacinto Fault, Southern California, from body waves recorded in dense linear arrays. *Journal of Geophysical Research: Solid Earth*, *119*(12), 8976–8990.

Yang, H., Yao, S., He, B., & Newman, A. V. (2019). Earthquake rupture dependence on hypocentral location along the Nicoya Peninsula subduction megathrust. *Earth and Planetary Science Letters*, *520*, 10–17.

Yang, H., & Zhu, L. (2010). Shallow low-velocity zone of the San Jacinto fault from local earthquake waveform modelling. *Geophysical Journal International*, *183*(1), 421–432.

Yao, S., & Yang, H. (2022). Hypocentral dependent shallow slip distribution and rupture extents along a strike-slip fault. *Earth and Planetary Science Letters*. https://doi.org/10.1016/j.epsl.2021.117296

Yoshimoto, K., Sato, H., & Ohtake, M. (1993). Frequency-dependent attenuation of P and S waves in the Kanto area, Japan, based on the coda-normalization method. *Geophysical Journal International*, *114*(1), 165–174.

Zhang, Y., An, Y., Long, F., Zhu, G., Qin, M., Zhong, Y., et al. (2022). Short-term foreshock and aftershock patterns of the 2021 Ms 6.4 Yangbi earthquake Sequence. *Seismological Research Letters*, *93*(1), 21–32. https://doi.org/10.1785/0220210154

Zhu, C. B., Thambiratnam, D. P., & Zhang, J. (2015). Seismic response of sedimentary basin subjected to obliquely incident SH waves. In *Proceedings of the 6th International Conference on earthquake Geotechnical engineering* (pp. 1–10). New Zealand Geotechnical Society.